Characterization of a kHz atmospheric pressure plasma jet: comparison of discharge propagation parameters in experiments and simulations without target

— Source link ↗

Marlous Hofmans, Marlous Hofmans, Pedro Viegas, Oliviern van Rooij ...+4 more authors

Institutions: Eindhoven University of Technology, École Polytechnique, Centre national de la recherche scientifique

Topics: Jet (fluid), Pulse (physics), Voltage, Atmospheric-pressure plasma and Electric field

Related papers:

- Guided ionization waves: Theory and experiments

- Atmospheric pressure plasma jets: an overview of devices and new directions

- On atmospheric-pressure non-equilibrium plasma jets and plasma bullets

- How dielectric, metallic and liquid targets influence the evolution of electron properties in a pulsed He jet measured by Thomson and Raman scattering

- Plasma-surface interaction: dielectric and metallic targets and their influence on the electric field profile in a kHz AC-driven He plasma jet

Characterization of a kHz atmospheric pressure plasma jet: comparison of discharge propagation parameters in experiments and simulations without target

Marlous Hofmans, Pedro Viegas, Olivier Van Rooij, Bart Klarenaar, Olivier Guaitella, Anne Bourdon, Ana Sobota

Characterization of a kHz atmospheric pressure plasma jet: comparison of discharge propagation parameters in experiments and simulations without target

To cite this article before publication: Marlous Hofmans *et al* 2020 *Plasma Sources Sci. Technol.* in press https://doi.org/10.1088/1361-6595/ab6d49

Characterization of a kHz atmospheric pressure plasma jet: comparison of discharge propagation parameters in experiments and simulations without target

Marlous Hofmans[1,2], Pedro Viegas[1]‡, Olivier van Rooij[2], Bart Klarenaar[2], Olivier Guaitella[1], Anne Bourdon[1] and Ana Sobota[2]

[1] LPP, CNRS, École Polytechnique, Sorbonne Université, Institut Polytechnique de Paris, 91128 Palaiseau, France
[2] EPG, Applied Physics, Eindhoven University of Technology, Postbus 513, 5600 MB, The Netherlands

E-mail: marlous.hofmans@lpp.polytechnique.fr; p.viegas@differ.nl; anne.bourdon@lpp.polytechnique.fr; a.sobota@tue.nl

16 December 2019

Abstract. This paper quantitatively characterizes a kHz atmospheric pressure He plasma jet without target powered by a pulse of positive applied voltage. It focuses on a quantitative comparison between experimental measurements and numerical results of a two-dimensional fluid model using the same configuration, for different values of magnitude and width of pulsed applied voltage. Excellent agreement is obtained between experiments and simulations on the gas mixture distribution, the length and velocity of discharge propagation and the electric field in the discharge front. For the first time in the same jet, the experimentally measured increase of the electric field in the plume is confirmed by the simulations. The electron density and temperature, measured behind the high field front, are found to agree qualitatively. Moreover, the comparison with simulations shows that discharge propagation stops when the potential in the discharge head is lower than a critical value. Hence, pulse width and magnitude allow to control propagation length. For long pulses ($\geq$ 1000 ns), the potential in the discharge front reaches this critical value during the pulse. For shorter pulses, propagation is determined

‡ Present address: DIFFER - Dutch Institute for Fundamental Energy Research, 5612 AJ Eindhoven, The Netherlands

Characterization of a kHz atmospheric pressure plasma jet: ... 2

by the pulse shape, as the critical value is reached around $90 - 130$ ns after the fall of the pulse. The results suggest that the magnitude of this critical value is defined by the gas mixture at the position of the front.

Keywords: plasma jet, benchmarking, electric field, electron density, discharge propagation, Thomson and Raman scattering, fluid model, atmospheric pressure

1. Introduction

Plasma jets are widely studied because of their broad range of applications such as medicine (e.g. wound healing and infection control [1]), agriculture [2] and surface modifications (e.g. on polymer fibres [3]). Although a plasma jet may look simple, it is in fact a transient discharge that is produced in a dielectric tube, through which it propagates in a flow of a rare gas (usually helium) that mixes with air at the end of the tube before it touches the target for the applications. For all these applications, as well as for the optimization of the plasma jet, it is important to understand the discharge dynamics of propagation in plasma jets. The electric field, electron density and electron temperature are important parameters to characterize the plasma jet propagation.

Although there have been some studies on the electric field [4], electron density [5, 6] and electron temperature [7] in jets, to our knowledge these parameters have never been experimentally assessed in one and the same free jet. To couple the results, it is important to measure them in the same jet. Moreover, comparison of experimental results with numerical simulations allows to validate diagnostics and models and to provide complementary information on each other. Also, there is an effort to increase the understanding of discharge dynamics through comparisons between simulations and experiments. So far, these comparisons focus mostly on evaluating tendencies and macroscopic parameters like discharge structure and light emission [8–13]. More recently, quantitative comparisons are performed on jets, focusing on ionization front propagation velocity [14,15], breakdown voltage [16] and electric field inside a dielectric target [17,18].

Concerning discharge dynamics of propagation in jets, the influence of different parameters has been addressed in several studies at atmospheric pressure. Firstly, studies have been performed on streamer discharges, which are relevant for the discharge propagation in jets, since it has been shown [19–24] that plasma jets are

Characterization of a kHz atmospheric pressure plasma jet: ... 3

ionization waves that propagate with the same mechanisms as streamer discharges in tubes and then in a plasma plume. In [25], two-dimensional positive streamer simulations in air have assessed these parameters. On the one hand, they have shown that the magnitude of the applied voltage determines the streamer dimensions, velocity and current. On the other hand, it has been reported that the electric field in the streamer head and in the plasma channel and the electron density in the channel do not change appreciably with the value of applied voltage. Moreover, in [26] it has been shown that the streamer velocity in air is proportional to the radius of the space charge layer in the discharge front.

Furthermore, in positive pulsed helium jets, [27] has revealed by fast photography that the time of ignition and velocity of propagation of the discharge are strongly dependent on the magnitude of the applied voltage and that the time at which the discharge stops propagating is set by the fall of the voltage pulse. Numerically, it has been reported in [28] that the velocity and length of propagation of helium plasma jets emerging in ambient air depend on the helium flow rate, thus on the helium-air mixing, and on the magnitude of the applied voltage. Furthermore, it has been shown experimentally in [29] that the discharge front leaves behind a quasi-neutral plasma channel, with a low electric field, that connects the potential in the powered electrode to that in the discharge front. In addition, through numerical simulations in [24] with a pure helium jet without air impurities and without helium-air mixing, the length of the discharge propagation has been related to the electric potential on the discharge head. In that work it has been estimated that the potential at the discharge front needs to be 2.75 kV for propagation to be maintained. Thus, it has been argued that the length of propagation is determined by the conductivity in the plasma channel, the value of applied voltage and the shape of the applied voltage.

In this work, some of the important plasma parameters (electric field, electron density and electron temperature) of the discharge propagation in a positive pulsed helium jet without target are measured and quantitative comparisons are performed with results from a two-dimensional fluid model. Furthermore, the criteria for discharge propagation and the end of discharge propagation are investigated.

In the coming sections, the experimental and numerical setups are discussed. In section 2.1, the experimental setup is described, together with the diagnostics used to determine the different plasma parameters. Section 2.2 exposes the numerical model, using the same configuration as in the experiments. Measurements of air

Characterization of a kHz atmospheric pressure plasma jet: ... 4

density confirm that the flow considered in the model is in agreement with the experiments. In section 3 the dynamics of discharge propagation are characterized through both experiments and simulations. The position of the discharge front, velocity of propagation, electric field in the discharge front and electron density behind the front are evaluated and directly compared. Finally, in section 3.3, experimental and numerical results of discharge propagation and electric field with different applied voltages and pulse widths are used to evaluate the criteria for discharge propagation. In particular, the electric potential on the discharge front required for propagation and the timescales on which it evolves with respect to the fall of applied voltage are assessed through the simulations.

2. Setup

2.1. Experimental setup

The atmospheric pressure plasma jet that is used in this work is the same as in [18,30–32] and it is shown in detail in figure 1. It consists of a pyrex capillary with an inner diameter of 2.5 mm and an outer diameter of 4 mm. A metal tube is placed inside, that functions both as anode and as inlet for the helium flow. A grounded metal ring with a width of 3 mm is placed around the capillary, 2 cm from the exit of the capillary and 5 mm from the anode. This ring is connected to the ground that is placed at least 20 cm from the jet. The plasma jet is operated vertically (downwards) and the piping in the setups is made of stainless steel to minimize the amount of impurities in the gas flow. It is powered by uni polar positive voltage pulses, for which the default settings are an amplitude V_P of 6 kV, a pulse length t_f of 1 μs and a repetition rate f of 5 kHz. The helium flow has a constant value of 1.5 slm. The voltage and current signals, measured at the anode with a high voltage probe (LeCroy PHV4-3432 14 kV AC) and a Rogowski coil (Pearson Current Monitor 6585) respectively, at these default settings are shown in figure 2.

Different diagnostics have been used to determine electrical, gas and optical properties of the plasma jet. An overview of these diagnostics with the parameters they provide is given in table 1. More information about the used diagnostics is given in the next paragraphs.

Characterization of a kHz atmospheric pressure plasma jet: ...
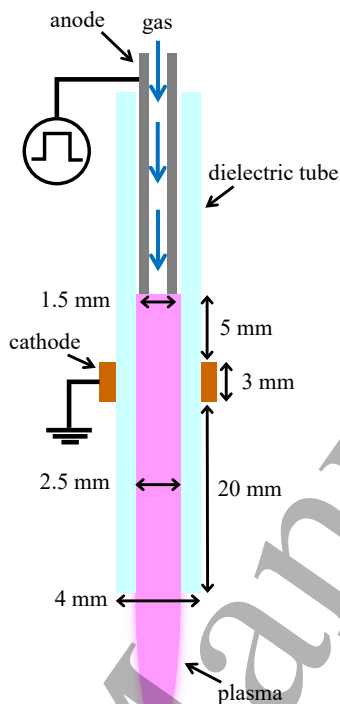
Figure 1. Schematic overview of the discharge setup used in the experiments.

Table 1. Used diagnostics, the resulting parameters of the plasma that are discussed in this work and references to more detailed explanations of the diagnostics.

Diagnostic	Resulting parameter(s)	Reference
Stark polarization spectroscopy	Electric field	[32]
Thomson scattering	Electron density and temperature	[33]
Rotational Raman scattering	Number density of oxygen and nitrogen	[33]
ICCD imaging	Position and velocity of ionization front	–

2.1.1. Stark polarization spectroscopy   For the electric field measurements, the Stark polarization spectroscopy setup is used that is described in detail in [32], with the adjustment that the $f_{\text{length}} = 15$ cm lens has been substituted by two $f_{\text{length}} = 12.5$ cm
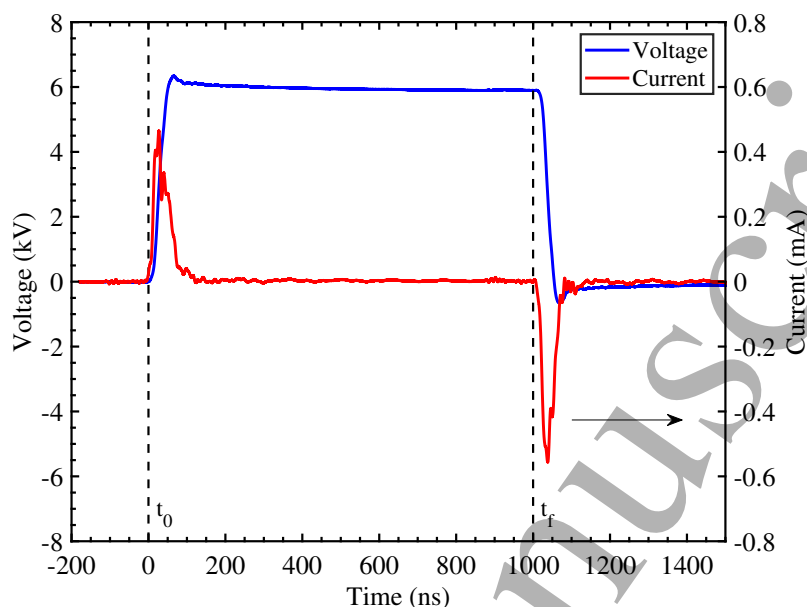
Figure 2. Applied voltage and current signals measured at the anode as a function of time, with $V_P = 6$ kV, $t_f = 1$ μs, $f = 5$ kHz, and 1.5 slm He.

lenses. The distances between the jet, lenses and spectrometer have been changed accordingly. Spectroscopy is performed on the helium 492.2 nm line, where the wavelength distance between the allowed and the forbidden component of the line determines the magnitude of the axial electric field in the ionization front, according to the calibration in [32]. The electric field is determined at the center of the jet along the vertical axis in figure 1, from inside the capillary just below the cathode up until about 2 cm in the effluent of the jet.

The images consist each of an on-chip accumulation of 20 frames that each integrate during 2 to 15 s every 10 ns long exposure that is triggered by the pulse of the jet. The integration time depends on the intensity of the signal. The slit width of the spectrometer was 100 μm.

2.1.2. Thomson and rotational Raman scattering The Thomson and rotational Raman scattering setup and analysis algorithms that are used in this work are described in more detail in [33–35]. For the measurements, the plasma jet is placed in the laser setup of [33] and a schematic of the setup can be found there. A Nd:YAG

Characterization of a kHz atmospheric pressure plasma jet: ... 7

laser (Spectra Physics, Quanta-Ray, Lab-190-100) is used with a frequency doubled wavelength of 532 nm, operating at 100 Hz with 140 mJ per pulse. Each laser pulse has a width of 100 μm at the focal point and a duration of 10 ns. The laser scattered light is captured at 90° to the laser path and the vertical axis of the jet, after which it is focused into a glass fiber. The Rayleigh stray light is removed by a volume Bragg grating (OptiGrate, BragGrate, BNF-532-OD4-12.5M) with a FWHM of 7 cm^{-1} [34] as Notch filter. The remaining Thomson and Raman scattered light is focused onto the 100 μm wide slit of the spectrometer (Jobin-Yvon, HR 640) that has a 1200 l/mm grating (Horiba, 530 24 Holographic Grating, blazed at 500 nm). Then, the spectrum is captured by a self-assembled ICCD camera (Allied vision BigEye G-132B Cool, with KATOD, EPM102G-04-22 F intensifier) integrating every exposure of 70 ns over 2.5 to 50 minutes, depending on the intensity of the signal. This spectrum has a frequency range of 510 cm^{-1} and a resolution of 0.398 cm^{-1} [33].

The obtained spectrum consists of the combination spectrum of the Thomson and Raman signals (example spectra are also shown in [33]). Both signals are Gaussian and are convolved with the Voigt instrumental broadening profile [33]. The total scattering power of the Thomson signal is proportional to the electron density n_e and the width is proportional to the square root of the electron temperature T_e [33,36]. The Raman signal is an addition of the individual rotational transitions of the molecules, in this case O_2 and N_2, from which the total scattering power is proportional to the density of O_2 and N_2, respectively [33,35,36]. More information about the calculations and algorithm to determine n_e, T_e, n_{O_2} and n_{N_2} can be found in [33,35]. Instead of taking the fitting error as the error in n_e, the error is determined from statistics, since this error is found to be the largest. Measurements at $z = 8.7$ mm are performed on different days and the resulting spread in the values for n_e of about 20% is taken as the error bar for all n_e measurements.

2.1.3. ICCD imaging The position and velocity of the ionization front in the plasma jet are determined by ICCD imaging. An ICCD camera (Standford Computer Optics 4Picos S20Q) is used to take images of the moving ionization front, increasing the delay time on the camera accordingly in steps of 20 ns, to follow the vertical movement of the front. Images are taken at an exposure time of 2 ns with an integration on chip of 10 to 20 exposures. The camera is triggered by the 5 kHz pulses that also drive the high voltage of the jet. In every consecutive image, the position and velocity of the ionization front are determined.

Characterization of a kHz atmospheric pressure plasma jet: ...   8

2.2. Numerical setup

The numerical setup is shown in figure 3. The geometry taken is the same as in the experiments (conform figure 1). A dielectric pyrex tube with a relative permittivity of $\epsilon_r = 4$, length 3.3 cm (between $z = 0.0$ cm and $z = -3.3$ cm), internal radius $r_{in} = 1.25$ mm and outer radius $r_{out} = 2.0$ mm is used. Helium flows through the tube with a 1.5 slm flux as in the experimental conditions. A free jet is studied, and thus no target is present, but a grounded plane is set far from the tube at $z = 20$ cm. A powered ring electrode of inner radius 0.4 mm and outer radius 1.25 mm is set inside the tube between $z = -2.8$ cm and $z = -3.3$ cm and a grounded ring is wrapped around the glass tube between $z = -2.0$ cm and $z = -2.3$ cm, at a distance of 0.5 cm from the inner ring. As in the experiments, the inner ring is powered by a positive applied voltage that rises from $t_0 = 0$ ns during 50 ns until reaching a plateau voltage V_P (as is shown in figure 2). Then, the applied voltage is constant until $t = t_f$ and decreases from there until $t_f + 50$ ns, when it reaches zero. Taking into account the high repetition rate in experiments ($f = 5$ kHz), we consider as in our previous works [17,18,37] that relatively high densities of electrons and positive ions remain in the discharge domain between pulses, as is also argued in [21]. Given the uncertainty on what the exact initial conditions should be to reproduce the repetitive discharges, we take into account a standard uniform initial preionization density n_{init} = 10^9 cm^{-3} of electrons and O_2^+. However, no initial surface charges are considered on the dielectric tube surface.

Figure 3 also shows that the discharge setup is placed inside a grounded cylinder with a radius of 10 cm. Between the dielectric tube and the grounded cylinder, the space is considered as a dielectric of air with permittivity $\epsilon_r = 1$. On the last boundary of the domain (i.e. at $z = -3.3$ cm), the axial gradient of the electric potential is set to zero. The simulations have been carried out in a cylindrically symmetrical computational domain at atmospheric pressure and at $T = 300$ K. A 2D axisymmetric fluid model is used to simulate discharge dynamics as in [18,37]. It is based on drift-diffusion-reaction equations for electrons, positive ions and negative ions and mean electron energy, and reaction equations for neutral species, coupled with Poisson's equation in cylindrical coordinates (z, r):

$$\frac{\partial n_i}{\partial t} + \nabla \cdot \mathbf{j_i} = S_i \tag{1}$$

$$\mathbf{j_i} = (q_i/|e|)n_i\mu_i\mathbf{E} - D_i\nabla n_i \tag{2}$$

Characterization of a kHz atmospheric pressure plasma jet: ...   9

$$\frac{\partial}{\partial t}(n_e \epsilon_m) + \nabla \cdot \mathbf{j}_\epsilon = -|q_e| \mathbf{E} \cdot \mathbf{j_e} - \Theta_e \tag{3}$$

$$\mathbf{j}_\epsilon = -n_e \epsilon_m \mu_\epsilon \mathbf{E} - D_\epsilon \nabla (n_e \epsilon_m) \tag{4}$$

$$\epsilon_0 \nabla \cdot (\epsilon_r \nabla V) = -\rho - \sigma \delta_s \tag{5}$$

$$\mathbf{E} = -\nabla V ; \rho = \sum q_i n_i \tag{6}$$

where $n_\epsilon = n_e \epsilon_m$ is the electron energy density, defined as the product of the electron density with the mean electron energy, Θ_e represents the power lost by electrons in collisions ($\Theta_e = P_{\text{loss}}/N_g(\epsilon) \times N_g \times n_e$) and j_ϵ is the flux of n_ϵ by drift and diffusion. The subscript i refers to each species and n_i, q_i, j_i, μ_i and D_i are the number density, the charge, the flux, the mobility and the diffusion coefficient of each species i, respectively. S_i is the total rate of production and destruction of species i by kinetic processes and by photoionization. V is the electric potential, $\mathbf{E}$ the electric field, e the electron charge, ϵ_0 the vacuum permittivity, ϵ_r the relative permittivity and δ_s the Kronecker delta (equal to 1 on the dielectric/gas interfaces). The electron temperature is $T_e = 2/3\epsilon_m$.
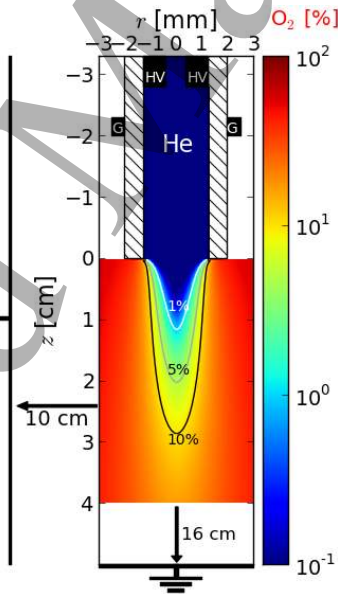

Figure 3. Side view schematics of the discharge setup used in the simulations. The colour plot and the contour curves show the O_2 spatial distribution in the He-O_2 mixture (percentage over a total of 2.45×10^{19} cm^{-3} gas density).

Characterization of a kHz atmospheric pressure plasma jet: ...   10

It is important to point out that at the surface of the tube, secondary emission of electrons by ion bombardment ($\gamma = 0.1$ for all ions) is taken into account. The surface charge density σ on the surface of the dielectric is obtained by time-integrating charged particle fluxes through electric drift to the surface. We consider that these charges then remain immobile on the surface of the dielectric. As in our previous works, the plasma model has been coupled with static flow COMSOL calculations [38, 39]. In this work, we use the same flow calculation as has been used in [30] with 1.5 slm of helium with 1000 ppm of air impurities flowing through the tube. In this work, we consider that helium contains O_2 impurities and flows downstream into an O_2 environment, as an approximation to air. Both experiments and simulations [40, 41] have shown that the use of O_2 or air as surrounding gas for a He jet present similarities with respect to discharge dynamics in the plasma plume. In [21, 41] the important role of the electronegativity of the surrounding gas, either O_2 or air, has been highlighted. Finally, in [39] (section III.6 and appendix F), attachment in oxygen has been shown to be relevant for the radial confinement of the discharge in the plume. The spatial distribution of O_2 in the He-O_2 mixture obtained from the flow calculation is presented in figure 3. The O_2 density in the model has been compared with radially-resolved Raman scattering measurements of the air density ($N_2 + O_2$). The comparison for two locations close to the tube exit, $z = 3$ mm and $z = 8.7$ mm, can be observed in figure 4 and shows that the flow calculations accurately reproduce the He-air mixture in the experiments for the region of interest: radial positions below 2 mm, which is the tube outer radius. Furthermore, it can be observed from the measurements that in that region the plasma has no effect on the flow.

The reaction scheme proposed in [37] has been used to describe the kinetics in the He-O_2 plasma. The scheme includes a total of 55 reactions with 10 species: e, O_2^-, He^+, He_2^+, O_2^+, He, $He(2^3S,2^1S)$, O, O_2, $O_2(a_1\Delta_g)$. The electron and electron energy transport parameters, power loss terms and rate coefficients of electron-impact reactions are calculated with the electron Boltzmann equation solver BOLSIG+ [42], using the IST-Lisbon database of cross sections in LXCat [43, 44], and tabulated as functions of both the local gas mixture and the local mean electron energy ϵ_m. In each cell and at each timestep, each coefficient k is calculated for the local values of the mixture and ϵ_m by linear interpolation between the local upper and lower tabulated values and we obtain k as a function of ϵ_m and the mixture, as in [39]. For the photoionization model, we use the approach described in [14, 18]. The ionizing

Characterization of a kHz atmospheric pressure plasma jet: ...   11
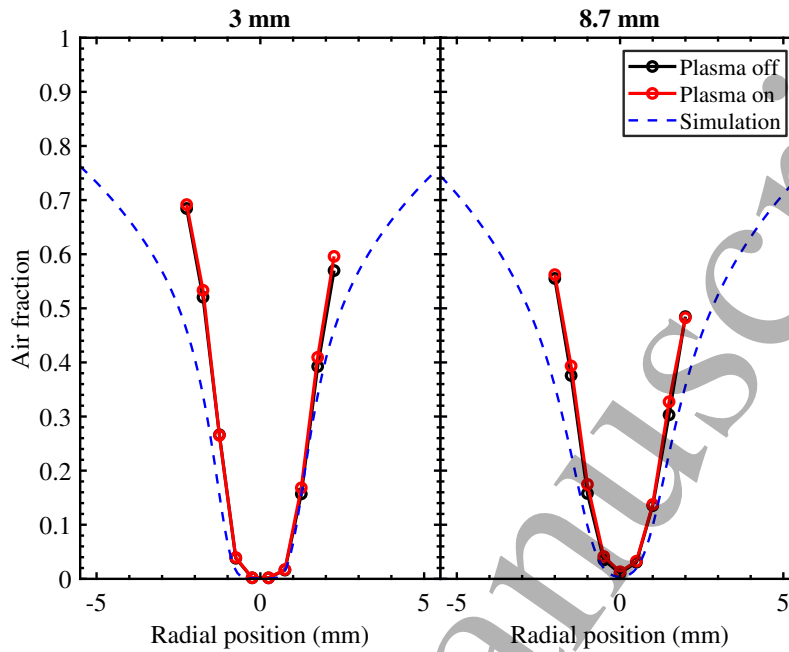
Figure 4.   Comparison of the air fraction in the flow from the COMSOL flow calculation with experimentally measured air fractions with and without plasma, as function of the radial position for $z = 3$ mm and $z = 8.7$ mm.

radiation is assumed to be proportional to the excitation rate of helium atoms by impact of electrons. The photoionization source term A_{ph} is proportional to the amount of O_2 admixture (X_{O_2}) and we use $A_{\mathrm{ph}} = \xi \times X_{O_2}$. In [39], we have varied ξ in the range of $10 - 1000$ for different plasma jet configurations. A small influence on the discharge structure and dynamics has been observed. In this work, $\xi = 100$ is used.

A finite volume approach and a Cartesian mesh are used. The mesh size is 10 μm, axially between $z = 5.0$ cm and $z = -3.3$ cm and radially between $r = 0$ and $r = 3.0$ mm. Then, both for $z > 5.0$ cm and for $r > 4.0$ mm, the mesh size is expanded using a geometric progression. The refinement taken requires a mesh of $\mathrm{n}_z \times \mathrm{n}_r = 8350 \times 370 = 3.090$ million points. The average computational time required for a 2 μs simulation run to obtain the results presented in this paper was of five days with 64 MPI processes on a multicore cluster "Hopper" (32 nodes DELL C6200 bi-pro with two 8-core processors, 64 GB of memory and 2.6 GHz frequency

Characterization of a kHz atmospheric pressure plasma jet: ... 12

per node). Further details on the numerical schemes and other characteristics of the simulations are given in [39].

3. Results and discussion

3.1. Characterization of discharge propagation and peak electric field

In this section and in the next section (section 3.2), the plasma jet operates at the default conditions: $V_P = 6$ kV, $t_f = 1$ μs, $f = 5$ kHz, and 1.5 slm He.

The propagation of the ionization wave as measured with ICCD imaging is shown in figure 5 for $t = 17 - 717$ ns with respect to the start of the pulse at $t_0 = 0$ ns as in figure 2. It can be seen that inside the tube, the ionization wave is wide and propagates along the walls towards the nozzle. When the ionization wave enters the ambient air, it is confined due to the mixing with the oxygen and nitrogen species in air. The discharge starts propagating from $z = -2.0$ cm around $t = 25$ ns, reaches
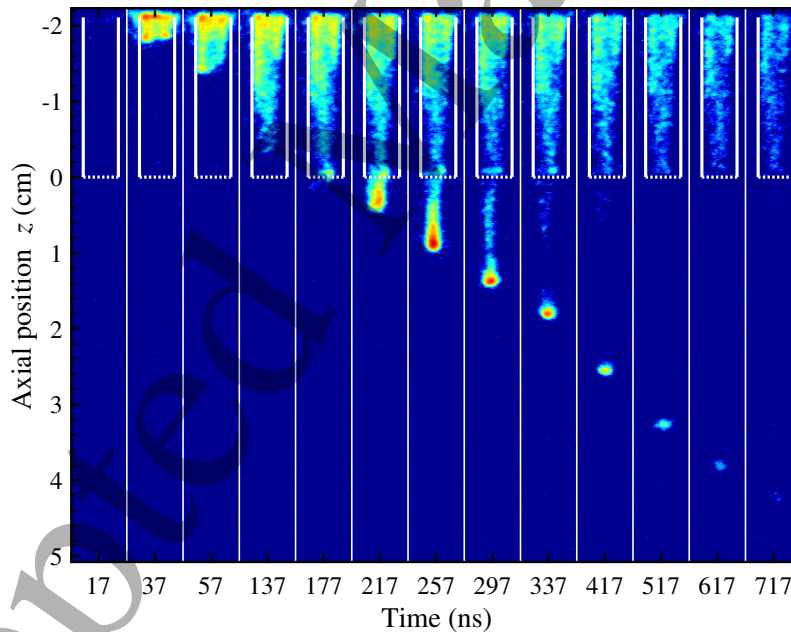
Figure 5. Images of the propagation of the ionization wave in space and time, with the colors, that represent the intensity of the light emission, plotted on a log scale. In these images, the jet operates at default conditions.

Characterization of a kHz atmospheric pressure plasma jet: ...   13
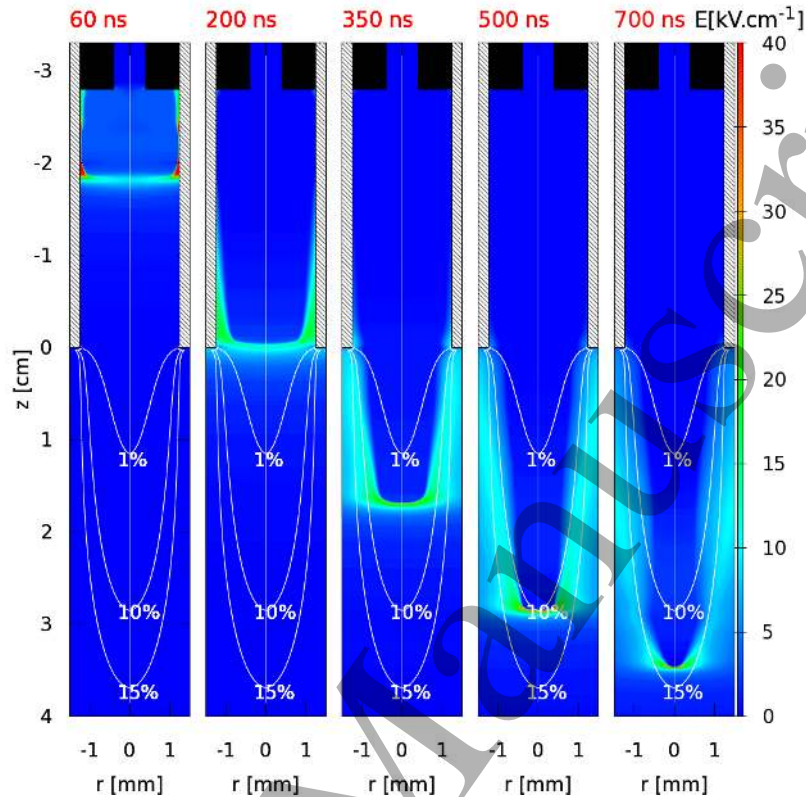
Figure 6. Cross sections of the spatial distribution of the electric field magnitude E_t from the simulations at different times. The contour curves show the O_2 spatial distribution in the He-O_2 mixture (percentage over a total of 2.45×10^{19} cm^{-3} gas density N_g).

the end of the tube around $t = 177$ ns and reaches the end of propagation at around $z = 4.0$ cm and $t = 617$ ns. Figure 6 shows the spatial distribution of the electric field magnitude from the simulations at different times. The peak of the electric field is located at the discharge front. Behind the front, there remains a quasi-neutral plasma channel with electron density in the order of $10^{12} - 10^{13}$ cm^{-3}. It is shown that the discharge crosses $z = -2.0$ cm around $t = 60$ ns in the simulations, while in the experiments this position is reached around $t = 25$ ns. The discharge fills the tube during propagation and reaches the end of the tube at around $t = 200$ ns. Thereafter, as in the experiments, the discharge is progressively radially confined as it propagates in the plasma plume, mostly due to higher electron-impact ionization

Characterization of a kHz atmospheric pressure plasma jet: ...   14

source term in the region with more helium and less molecular gases. A more detailed study of the mechanisms leading to the radial confinement in the plume has been carried through in [39] (section III.6). Finally, the end of discharge propagation is reached at around $t = 700$ ns and $z = 3.5$ cm, where the gas-mixture at $r = 0$ mm is close to 86% He + 14% O_2.

To study and quantify the propagation of the discharge better, the axial position of the ionization wave as a function of time and the velocity as function of position are shown in figure 7(a) and figure 7(b), respectively, where an average agreement between measurements and simulations within 5 mm at the position and of about 80% in the velocity is shown. The position and velocity of the ionization front in the simulations is obtained by following the maximum of the magnitude of the axial electric field E_z every 10 ns. There is a small difference in ignition time between the experiments and the simulations: in the experiments the discharge starts propagating from $z = -2.0$ cm at around 25 ns, while in the simulations this takes place around $t = 60$ ns. In the experiments, the discharge has a repetition rate of 5 kHz, while the simulations contain only one pulse. The difference between experiments and simulations is attributed to the uncertainty in memory effects, such as the possibility of leftover surface charges between pulses on the inner surface of the dielectric tube, that are not taken into account in the model.

In figure 7(a) it can be seen that the difference between the experimental and numerical axial position of the ionization front stays approximately constant during the propagation. Thus, the discharge takes the same amount of time in the experiments and simulations to propagate from the grounded electrode to the nozzle and from the nozzle to its maximum propagating distance of 3.5 cm at about 600 ns. Since the length t_f of the applied voltage pulse is 1000 ns, it can be noticed that the discharge stops propagating before the voltage pulse has ended. After $t = 600$ ns, the discharge in the experiments is too faint for light to be captured with the camera. We can conclude that the propagation length agrees well within 5 mm.

About the velocity results in figure 7(b), the first data point corresponds to a time of 37 ns in the experiments, while in the case of the simulations it has been obtained from the difference between the positions at 60 and 70 ns. The experiments and the simulations show the same behaviour. The velocity starts at a high value of about 1.8×10^5 m/s and decreases until the end of the tube. This can be attributed to the increasing distance between the front and the powered electrode [39] (section III.2) or to the charge losses to the tube walls [32, 45]. When the ionization wave

Characterization of a kHz atmospheric pressure plasma jet: ... 15

enters the ambient air, the velocity first increases and then decreases again until the discharge reaches its maximum propagating distance, where the velocity drops to zero
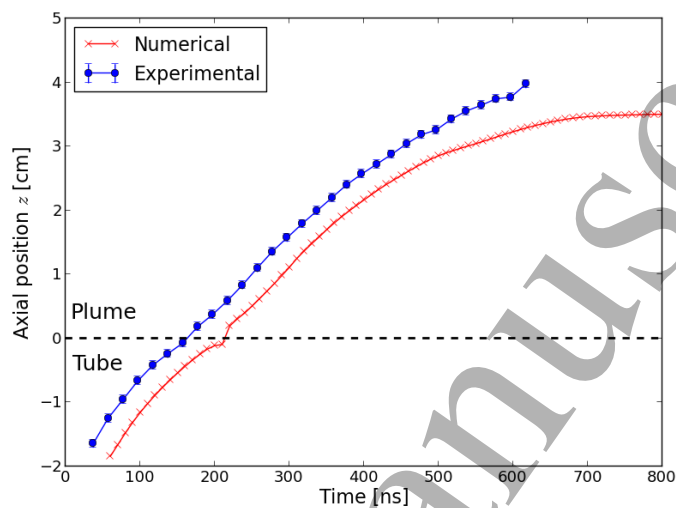
(a)
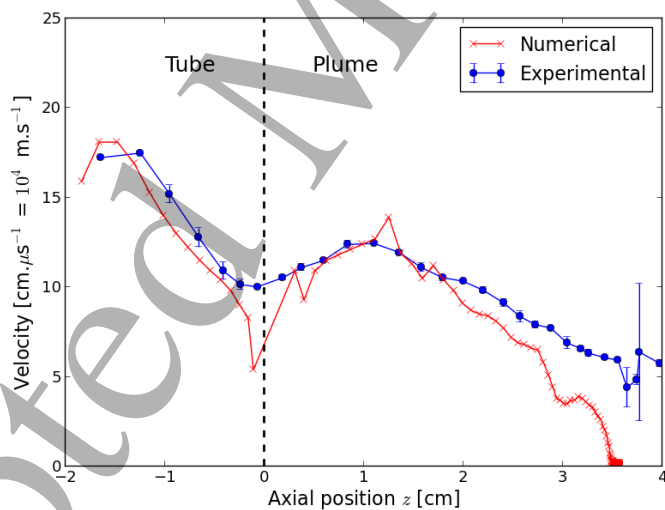
(b)

Figure 7. Results from the experiments and simulations on a) the position of the discharge as a function of time, and b) the velocity of the discharge during axial propagation in the tube and the plume.

Characterization of a kHz atmospheric pressure plasma jet: ...   16

in the simulations and becomes immeasurable in the experiments. This behaviour
was also observed in other experiments [10, 46–48] and simulations [24, 49, 50]. There
are two effects that can play a role to explain this behaviour. First, as explained
in [46], when entering the ambient air, the discharge ionizes and excites the N_2
and O_2 species in the air. Close to the nozzle there is enhanced plasma chemistry,
due to the influence of the applied voltage and He metastables that induce Penning
ionization of N_2 that has a lower ionization energy than He. Therefore, the velocity
of the discharge increases in the first cm of the plume. Further away, the influence of
the applied voltage decreases and thus the velocity too [46]. The radial confinement
itself of the discharge can also contribute to the decrease of the velocity, since it was
shown in [26] that the radius of the discharge front is proportional to the streamer
velocity in air. Second, as shown in [50] with simulations of pure helium in tubes
with varying permittivity, a change in permittivity from $\epsilon_r = 4$ (the tube) to $\epsilon_r = 1$
(the ambient air) causes the velocity to rise. No He/air mixing or Penning ionization
were taken into account in these simulations, making the difference in permittivity
the main cause for the increasing velocity that has been observed.

The discharge propagates because of charge separation at the high electric field
front. In figure 8, the maximum of the axial component of the electric field $E_{z\mathrm{MAX}}$ as
function of axial position is shown from both the experiments and the simulations.
In both cases, $E_{z\mathrm{MAX}}$ is the peak electric field in the center of the front [32], with a
radial uncertainty of the size of the slit width of 100 μm. In the simulations, $E_{z\mathrm{MAX}}$ is
obtained with a 1 ns resolution. As explained in [32], $E_{z\mathrm{MAX}}$ in the experiments comes
from the distance between the allowed and forbidden line of the studied helium band,
where the position of the forbidden line changes the most due to the high electric
field. The uncertainty of the fit in determining the wavelength position of both lines
is used as the error, yielding an error in the electric field values of around ± 1 kV/cm,
as can be seen in figure 8. This means that the $E_{z\mathrm{MAX}}$ we measure might not be the
highest at the measured position, but actually an average value and the real value
lies within a range of ± 1 kV/cm. In the simulations, a range of ± 1 kV/cm around
the maximum E_z corresponds to a distance of around $z \pm 0.1$ mm around the position
of this E_z. Therefore, we take the average E_z within a distance of ± 0.1 mm around
z, and this is the red curve that is shown in figure 8. This average corresponds better
to the experimentally obtained values than the absolute $E_{z\mathrm{MAX}}$ from the simulations.

There is no experimental data of $E_{z\mathrm{MAX}}$ for $z > 2.0$ cm present in figure 8,
because the intensity of the discharge is too low to obtain a fittable spectrum here.

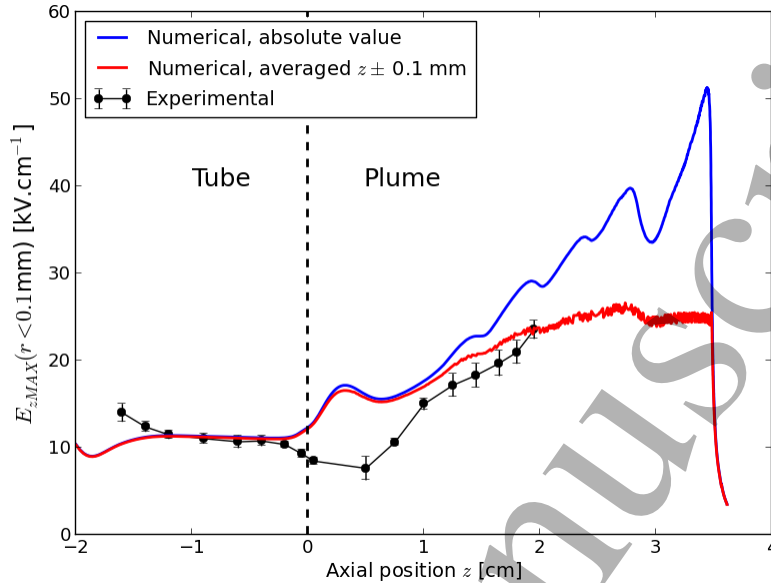*Characterization of a kHz atmospheric pressure plasma jet: ...*   17

Figure 8. Maximum axial component of electric field E_z for $r < 0.1$ mm at the discharge front during propagation in the tube and the plume, in experiments and simulations.

For the other positions, the agreement in $E_{z\mathrm{MAX}}$ obtained from the experiments and from the simulations shows a discrepancy up to a maximum of 11%, with $E_{z\mathrm{MAX}}$ around 10 kV·cm^{-1} inside the tube and rising up to 20 kV·cm^{-1} in the plume. A larger difference can only be seen just outside the tube, where $E_{z\mathrm{MAX}}$ shows a decrease in the experiments, but an increase in the simulations. This increase may be due to the change of permittivity between the tube with $\epsilon_r = 4$ and the ambient air with $\epsilon_r = 1$ [50]. The fact that the tube edges are sharp in the model, while they are rounded in the experiments, might account for the difference. From imaging (figure 5) it can also be seen that the discharge is slightly wider close to the nozzle than further away. The highest value of the electric field at z positions close to the nozzle might then radially be just off-center. Since in the experiments $E_{z\mathrm{MAX}}$ is measured at $r = 0$ mm, this measured value might be lower than the highest electric field value at these z positions, thus contributing to the difference in $E_{z\mathrm{MAX}}$ between the experiments and the simulations at positions close to the nozzle.

The experimental results of $E_{z\mathrm{MAX}}$ are similar to previously published

experimental results without target [32], and also for a plasma jet with a different geometry [51,52] or a different shape of the applied voltage [30,53]. $E_{z\text{MAX}}$ increases when the discharge propagates through the ambient air, in both the experiments and the simulations. Thus, this trend of the electric field from experiments is confirmed and quantitatively compared with simulations on the same jet configuration. The simulations also allow an explanation for this behaviour. With the admixture of molecular gases along the plume, the electron-impact ionization coefficient decreases [20] and the losses of electrons through recombination and attachment increase (see [39] (section III.6)). Thus, the peak electric field required to produce free electrons ahead of the discharge front effectively enough to sustain discharge propagation increases along the plume. The volume where this production is effective is dependent on the gas-mixture and decreases along the propagation in the plume, leading to the radial confinement observed in figure 5 and figure 6.

3.2. Characterization of electron density and temperature

The axial profiles of the electron density n_e and electron temperature T_e along the propagation are shown in figure 9(a). In the experiments, these are determined with a 10 ns laser pulse around the center of the ionization wave that propagates at a velocity of about 1.0×10^5 m/s (see figure 7(b)), meaning that the ionization wave propagates over about 1 mm during the laser pulse. Therefore, n_e is found in the simulations by looking every 10 ns for the maximum of E_z and then searching the maximum n_e within a 1 mm distance from this position. T_e is found in the simulations at $r = 0$ mm and axially 0.5 mm behind the position of the maximum of E_z. This is a way to make sure that T_e lies in the quasi-neutral plasma channel, and not in the region of charge separation where gradients are very strong. The results show a qualitative agreement, as n_e increases and T_e decreases in the plume in both experiments and simulations. Yet, discrepancies are visible, reaching up to a factor 4. The increase of n_e in the plume is expected and is in correspondence with the behaviour of the electric field in figure 8. Several simulations [21, 28, 54, 55] and experiments [5, 6, 33] have observed this increase too. Moreover, the obtained values of T_e are similar to other simulations [56] and experiments [5, 7].

Several jet simulation results in the past have reported electron density values lower than those experimentally observed here. In [21], simulations have been done on a jet that is powered at 7 kV and where 7 slm He flows through a 3 mm wide

Characterization of a kHz atmospheric pressure plasma jet: ... 19

tube into air. The obtained values for n_e are 0.75×10^{12} cm^{-3} just outside the tube and 1.6×10^{12} cm^{-3} at $z = 4$ cm. These values are lower than the simulation values in our case. For a similar jet, powered at 4 kV, n_e values of 0.2×10^{12} cm^{-3} have been obtained just outside the tube and 6.7×10^{12} cm^{-3} at 1.3 cm from the nozzle
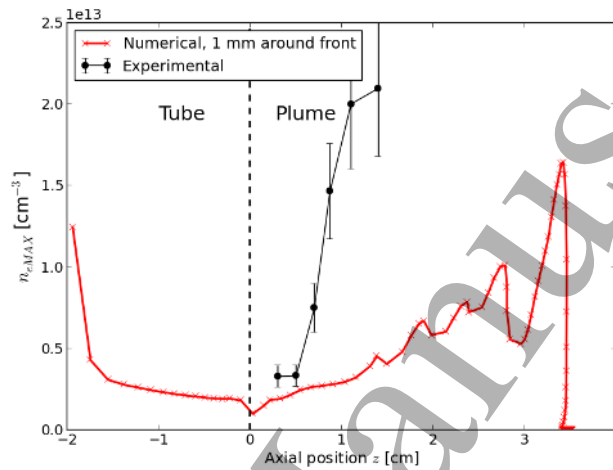
(a)
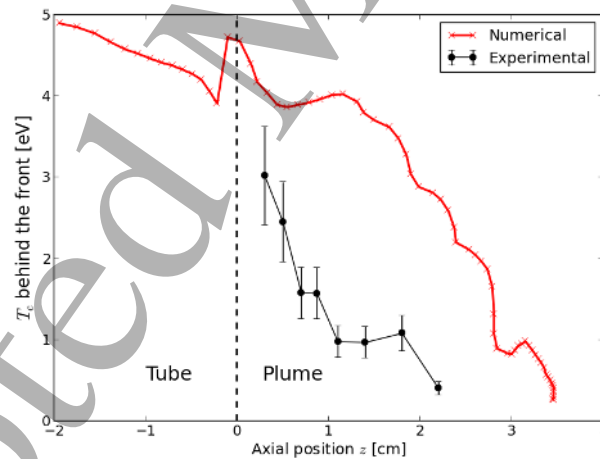
(b)

Figure 9. a) Electron density, and b) electron temperature, behind the discharge front during propagation in the tube and the plume, in experiments and simulations.

in the simulations in [28]. This first value is lower than our simulation values and the second value compares better to $z = 1.8$ cm in our case. The n_e that have been obtained in [24], for a 4 kV powered jet where He flows through a tube with 2 mm inner diameter into N_2 with no He/N_2 mixing taken into account, are 0.2×10^{12} cm^{-3} at $z = 0.5$ cm and 0.7×10^{12} cm^{-3} at $z = 3$ cm. Both these values are lower than n_e obtained in our simulations. A jet where 2 slm He is flowing through an ≈ 0.8 mm wide tube into air and that is powered with 130 ns long -10 kV pulses is used in [11]. There, the highest value of 5×10^{12} cm^{-3} was found in the plume, which corresponds to our value in the simulations at $z = 1.5$ cm. Recently, simulations were done on a jet interacting with different targets [54]. Powered by 200 ns long 8 kV pulses, 3 slm He was flowing into a humid air atmosphere and the targets were placed at $z = 17$ mm. With a non conductive, dielectric target, n_e values were found of 1.2×10^{12} cm^{-3} just outside the tube and 2.4×10^{12} cm^{-3} in the vicinity of the target. With a grounded metal target, n_e increases to 7.5×10^{12} cm^{-3} just outside the tube and 9×10^{12} cm^{-3} in the vicinity of the target. The n_e obtained from our simulations without a target fit in between the results for these targets, since our values are larger than the results for the dielectric target, but smaller than the grounded metal results.

The experimental values for n_e in this work agree with already published results [33], where the same jet was used. At $z = 0.3 - 0.5$ cm, the experimental n_e of around 0.4×10^{13} cm^{-3} is similar to n_e at $z = 0.2$ cm in [5], where an AC-powered jet is used with a slightly different geometry. Therefore, not the full axial profile is similar and their measured value of 0.8×10^{13} cm^{-3} at $z = 1.1$ cm corresponds more to $z = 0.7$ cm in our case. A different jet was used in [6], with a smaller nozzle diameter of 1 mm, a lower flow of 1 slm He and powered by 150 ns long 9 kV pulses. The experimentally obtained values for n_e in [6] are 1.5×10^{13} cm^3 at $z = 1$ mm and 2.0×10^{13} cm^{-3} at $z = 5$ mm, that correspond to our experimental n_e at $z = 8.7$ mm and $z = 11$ mm, respectively. Thus, in general the obtained n_e are similar to results from literature, but the experimentally obtained values are higher than the values obtained from the simulations.

To be certain of the validity of the experimental results for n_e and T_e, a number of things has been checked. During the experiments, the laser intensity is constantly monitored, but no irregularities could be found in these results: the laser intensity was approximately constant during all measurements. Also, measurements have been done at the same conditions, but at different times and days. The obtained results are constant within the error bars, thus the measurements are reproducible. In the

Characterization of a kHz atmospheric pressure plasma jet: ...   21

spectra and fits of all measurements, no irregularities are visible. At least once per day, a calibration of the laser setup is performed: switching the plasma and the helium flow off, a measurement is taken of the ambient air at the position of the jet. Knowing the ratio of N_2 and O_2 in air, this gives us the relation between the intensities of N_2 and O_2 in the total spectrum and their densities. From the measured spectra of that day, the densities of N_2 and O_2 can then be calculated.

An important difference between the simulations and the experiments is the presence of the laser pulse. We have not observed distortion of the plasma by the laser: using (ICCD) imaging and current-voltage characterization, the plasma looked the same with the laser on as with the laser off. However, according to [57] the high intensity of the laser might ionize Rydberg states, leading to a higher measured n_e in the experiments. To account for the discrepancy of almost one order of magnitude, it would mean that the density of these Rydberg states has to be in the order of 10^{13} cm^{-3}. According to the simulations, the density of helium metastables He* in the jet is in the order of 10^{12} cm^{-3} [17,37]. Since the Rydberg states have a higher energy level than He*, it is reasonable to assume that their population density would be even lower in the absence of a preferred population channel for the Rydberg states. Therefore, the ionization of Rydberg states cannot account for the one order of magnitude discrepancy. It could also be possible that the laser is photodetaching electrons from O_2^-, leading to a higher electron density. However, the density of O_2^- is never exceeding 10^{12} cm^{-3} [37], which is too low to account for the discrepancy.

Another difference is that in the simulations only oxygen species are taken into account and no nitrogen species. N_2 is together with He* via Penning ionization an efficient source of electrons. Although O_2 takes part in Penning ionization too, it is also efficient in electron attachment. Therefore, the simulations may overestimate the attachment. To account for that difference, simulations have been performed with Penning ionization enhanced by a factor 10 and with attachment decreased by a factor 5. Although the enhanced Penning ionization can increase n_e by a factor 2, these changes cannot reproduce the experimental values of n_e. As argued before, there is also an uncertainty in the memory effect of the discharge.

Further insight into the spatial gradients of n_e and T_e during discharge propagation is obtained through the 2D spatial distribution of these quantities from simulation results at $t = 400$ ns, represented in figure 10. It shows that at each moment, these quantities are highly dependent on the position, both radially (with respect to the center) and axially (with respect to the front). Figure 11 shows
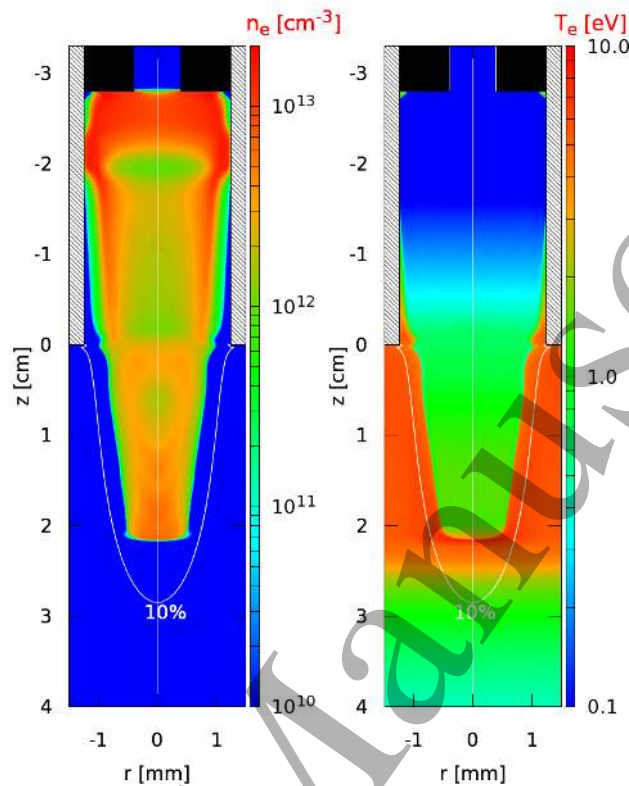
Characterization of a kHz atmospheric pressure plasma jet: ... 22

Figure 10. Cross sections of the spatial distribution of the electron density n_e and electron temperature T_e from the simulations at $t = 400$ ns.

simulation results of the axial profile of E_z, n_e and T_e in the discharge front region at $r = 0$ mm and $t = 500$ ns. It is shown clearly that E_z and T_e are high at the discharge front, but are significantly lower behind the front, in the region where n_e is the highest. Indeed, the maxima of E_z and T_e are both located around $z = 2.85$ cm, while the maximum of n_e is around 0.5 mm behind this position (around $z = 2.80$ cm). These simulation results suggest that the Thomson measurements assess the region behind the front, where n_e is high and T_e is low, and that the measurements in this region are not proportional to the peak of T_e. Behind the front, quasi-neutrality leads to a low electric field and therefore to a low acceleration of the electrons (according to the $-|q_e|\mathbf{E} \cdot \mathbf{j_e}$ term in equation (3)). Simultaneously, the higher density of electrons and of molecular gases leads to higher losses of electron energy through collisions (the $-\Theta_e$ term in equation (3)). These factors justify why T_e is higher ahead of the front

than behind the front. Moreover, they explain the decrease of T_e behind the front as the discharge propagates along the plume, that is registered in both experiments and simulations in figure 9. As $E_{z\mathrm{MAX}}$ increases along the plume (figure 8), the electron production increases too and the increase of n_e leads to a decrease of T_e behind the front. The results of figure 11 also indicate that the criteria used to choose the locations of the numerical n_e and T_e to compare with experiments in figure 9 are appropriate.
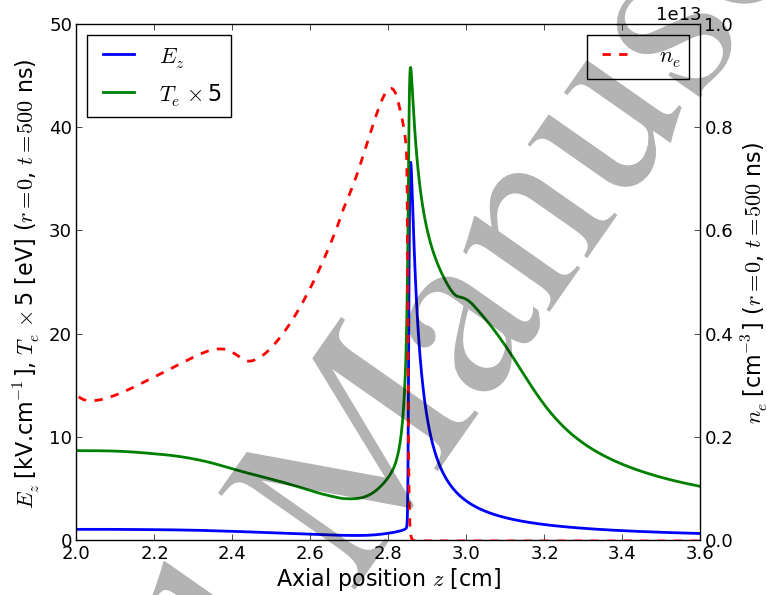
Figure 11. Axial profiles of E_z, T_e and n_e at $r = 0$ mm, from the simulations at $t = 500$ ns.

3.3. End of discharge propagation

The previous sections have shown that the discharge propagates up to 4 cm after the end of the tube and stops propagating before the end of the applied voltage pulse, both in the experiments and in the simulations. In this section, we change the magnitude of the applied voltage V_P and the pulse width t_f, and study their effect on the discharge propagation. In [18] these two parameters have been shown to determine the charging time of a jet impacting on a dielectric surface and thus the

Characterization of a kHz atmospheric pressure plasma jet: ... 24

electric field experienced by the surface. Figure 12 presents the temporal evolution of the axial position of the discharge front during its propagation, in experiments and simulations, for $V_P = 6$ kV and pulse width $t_f = 300$, 400 and 1000 ns. Moreover, the case with $V_P = 4$ kV and pulse longer than the time of propagation is also shown. In the simulations, the propagation at $V_P = 4$ kV takes slightly longer than 1000 ns. In the experiments, the propagation ends sooner in this case and is not affected by the fall of the pulse. Thus, to be sure that the fall of the pulse in this case does not interfere with the end of propagation, we have taken $t_f = 2000$ ns instead of 1000 ns in the simulations. In the experiments, the position is obtained by imaging and in the simulations by following the maximum of $|E_z|$ every 1 ns.
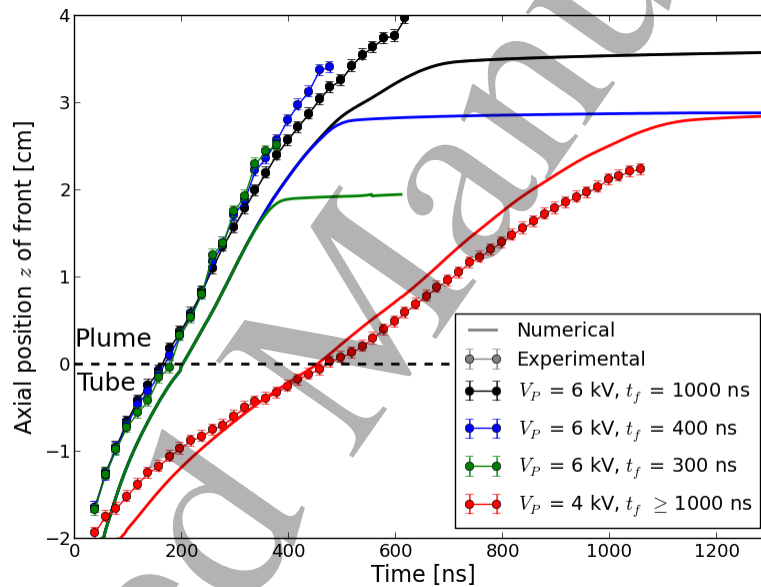
Figure 12. Temporal profile of axial position of discharge front during propagation in the tube and in the plume, in experiments and simulations, for several cases of V_P and t_f.

In agreement with [18, 25–28], figure 12 shows that the discharge with a lower applied voltage propagates slower. Moreover, it confirms through both experiments and simulations the later time of ignition with lower applied voltage reported in [27]. As in the previous section, ignition (time when the discharge has been formed and begins propagating beyond the grounded ring) takes place earlier in experiments

Characterization of a kHz atmospheric pressure plasma jet: ...   25

than in simulations. It is visible in figure 12 that for most cases the difference in experimental and numerical position of the discharge front stays approximately constant, which shows that the velocity of propagation is very similar in experiments and simulations. The length of propagation in experiments and simulations also presents an agreement within 5 mm. With $V_P = 6$ kV, the discharge propagates in every case about 0.5 cm longer in the experiments than in the simulations, while with $V_P = 4$ kV the length of the plume is about 0.5 cm shorter.

Figure 12 also shows that the discharge with $V_P = 6$ kV and $t_f = 1000$ ns stops propagating at around $t = 600$ ns in experiments and $t = 700$ ns in simulations. In both cases, the end of discharge propagation takes place during the pulse, when the applied voltage is still 6 kV. When the pulse is shortened, we observe that the time and position of the end of propagation are also shortened, in both experiments and simulations. In fact, the discharge propagation is the same for every case with $V_P = 6$ kV, until later than $t = t_f$. When t_f is lower than the natural time of discharge propagation, the fall of the pulse of applied voltage forces the discharge to stop propagating, as reported in [27]. Furthermore, decreasing V_P from 6 to 4 kV also leads to a shorter discharge propagation. As happened in [18] with a discharge-target interaction, also the discharge propagation can be controlled through pulse width and magnitude of applied voltage. In figure 13 we study the evolution of the electric field on the discharge front for three different cases of V_P and t_f to evaluate its relationship with the end of discharge propagation. The maximum electric field from the simulations is obtained every 5 ns in the region with $r < 0.1$ mm and is averaged over 0.2 mm axially.

Firstly, figure 13 shows that in experiments the electric field on the ionization front is approximately the same for different V_P and t_f, all along the propagation, in agreement with [25]. The simulation results show values very close to the experimental ones, except for the 1 cm region after the end of the tube, and also reveal very close electric field values for different V_P and t_f, until the end of discharge propagation. It is shown in figure 13 that when the discharge stops propagating, whether during the pulse or after the fall of the pulse, the maximum electric field decreases very rapidly. In fact, the electric field increases during propagation in the plume and then, once the discharge stops propagating, the maximum electric field decreases from about 25 kV·cm^{-1} to 10 kV·cm^{-1} in around 100 ns. Hence, the end of discharge propagation is not determined by a slow decrease of electric field in the ionization front. As in [24], we relate the discharge propagation with the electric

Characterization of a kHz atmospheric pressure plasma jet: ... 26
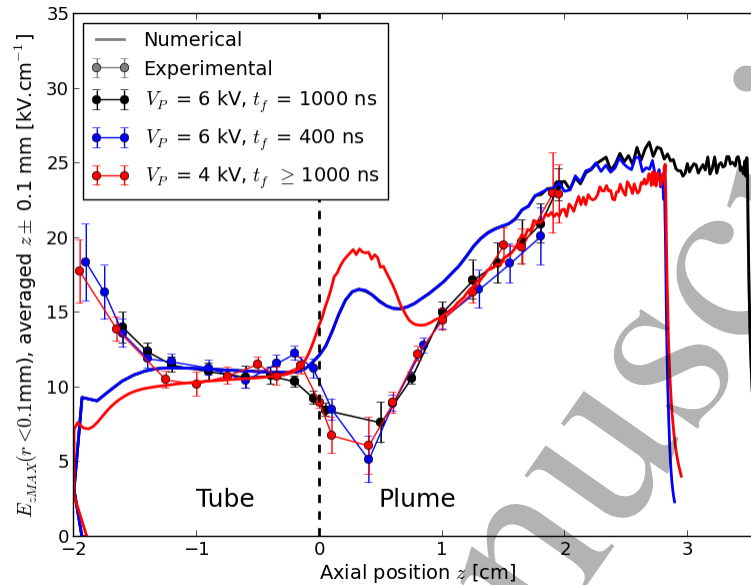

Figure 13. Maximum axial component of electric field E_z for $r < 0.1$ mm at the discharge front during propagation in the tube and the plume, in experiments and simulations, for several cases of V_P and t_f.

potential in the discharge front. Figure 14 presents the temporal evolutions of the applied voltage (V_{app}) and the electric potential in the discharge front (V_{head}) from the simulations for every case of V_P and t_f. V_{head} is identified by taking the electric potential at $r = 0$ mm and axially 0.5 mm behind the position of the maximum of $|E_z|$. Thus, V_{head} is at a position in the quasi-neutral plasma channel, and not in the region of charge separation where the gradient of electric potential is very strong.

During propagation, the discharge front leaves a quasi-neutral plasma channel behind, with a low electric field, that connects the potential in the powered electrode to that in the discharge front. Figure 14 shows that with $V_P = 6$ kV, the electric potential in the discharge front slowly decreases during the propagation and with $V_P = 4$ kV it stays almost constant until around 1200 ns, which is after the end of propagation. With $V_P = 6$ kV and $t_f = 1000$ ns, the slow decrease continues even after the discharge has stopped propagating at around $t = 700$ ns. Then, in every case, it is visible that the potential in the discharge head is forced to decrease at the end of the pulse. However, figure 14 shows that the decrease takes place with some
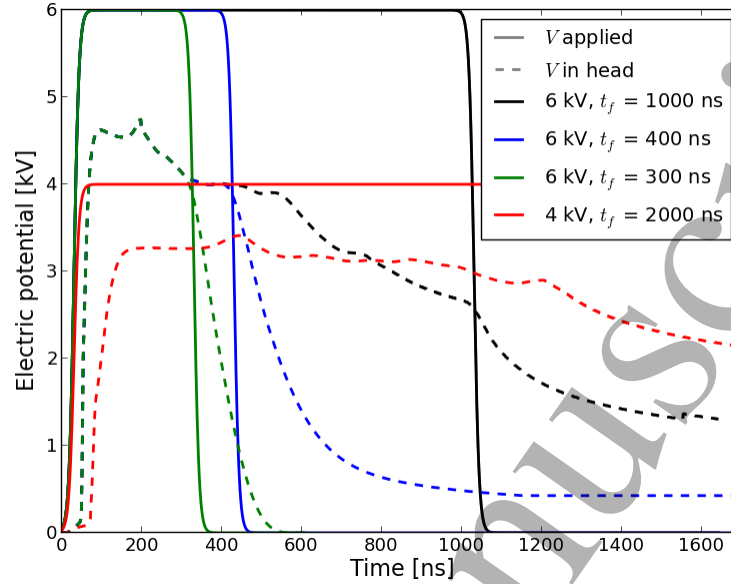
Characterization of a kHz atmospheric pressure plasma jet: ... 27

Figure 14. Temporal profile of applied voltage and electric potential in discharge front, in simulations, for several cases of V_P and t_f.

delay, and so does the end of propagation. That delay is variable, as it is shown that the fall of V_{head} after the end of the pulse is slower when V_{head} at $t = t_f$ is lower and thus more losses are present along the channel.

Table 2 reports on the parameters of propagation from simulations for several cases of V_P and t_f. For every case of V_P and t_f, the time of end of discharge propagation t_{stop} has been found by identifying the axial velocity of propagation as being $\leq 0.1 \times 10^5$ m/s, with a 10 ns resolution. The axial position of the maximum of $|E_z|$ at $t = t_{\text{stop}}$ is called z_{stop}. The electric potential 0.5 mm behind z_{stop}, V_{head}, and the relative density of O_2 in the He-O_2 mixture at $z = z_{\text{stop}}$ and $r = 0$ mm have also been found and tabulated. V_{head} in this table provides an estimation of the electric potential in the discharge front required to propagate.

Table 2 shows that with short pulses ($t_f < 1000$ ns) the discharge propagation stops always between 90 and 130 ns after the beginning of the fall of the pulse (t_f). With long pulses ($t_f \geq 1000$ ns) the propagation ends during the pulse. It also shows that in the cases with $t_f < 1000$ ns the potential in the discharge front V_{head} at t_{stop} is lower than V_{head} at t_f (figure 14), which clearly shows the influence of the fall of

Characterization of a kHz atmospheric pressure plasma jet: ...　　　　28

Table 2. Time, position, electric potential and oxygen relative density in discharge front at $r = 0$ mm at moment of end of propagation, for several V_P and t_f.

V_P [kV]	t_f [ns]	t_{stop} [ns]	z_{stop} [cm]	$[O_2]/N_g$ [%]	V_{head} [kV]
6	300	400	1.90	4.34	1.92
6	400	520	2.80	9.68	2.31
6	600	690	3.44	13.53	2.67
6	1000	700	3.47	13.71	3.23
5	600	730	2.82	9.80	2.34
5	1000	840	3.12	11.62	3.11
4	600	720	1.17	1.04	1.71
4	2000	1130	2.79	9.62	2.87

applied voltage. In [24] it has been suggested that V_{head} required to propagate is close to 2.75 kV. Here, it is shown that this value is variable and proportional to the relative density of O_2 at $z = z_{stop}$ and $r = 0$ mm. The obtained values are in the same range as the value proposed by [24]. V_{head} required for the discharge to propagate is represented in figure 15 as function of the relative density of O_2 at $z = z_{stop}$ and $r = 0$ mm, from all the cases in table 2. In fact, with the admixture of O_2, the electron-impact ionization coefficient decreases [20] and the losses of electrons through recombination and attachment increase [39] (section III.6). The peak electric field required to produce free electrons ahead of the discharge front effectively enough to sustain discharge propagation increases along the plume. On the one hand, that electric field is dependent on the electric potential in the plasma. On the other hand, it is generated by charge separation, which is directly affected by the chemistry in the local gas-mixture. Hence, the combination of the two factors determines if a high enough electric field can take place and in which volume it effectively produces free electrons to sustain discharge propagation. The higher the mixing of O_2 in helium, the more difficult it is to obtain the charge separation necessary to produce the required electric field to sustain propagation and thus V_{head} required for the discharge to propagate is higher. Figure 15 shows that the relationship between V_{head} required for the discharge to propagate and $[O_2]/N_g$ is approximately linear for the cases where the discharge is forced to stop propagating by the fall of the applied voltage ($t_f < 1000$ ns) and can be formulated as

$$V_{head} = 0.076 \times [O_2]/N_g + 1.606 \tag{7}$$

Characterization of a kHz atmospheric pressure plasma jet: ...   29

with $[O_2]/N_g$ in % and V_{head} in kV. For long pulses ($t_f \geq 1000$ ns), as the applied voltage still has an influence on the potential in the plasma at the moment when the discharge stops, V_{head} is higher than in equation (7) but can also be approximately expressed by a linear relationship with $[O_2]/N_g$ in the front:

$$V_{head} = 0.084 \times [O_2]/N_g + 2.087 \tag{8}$$

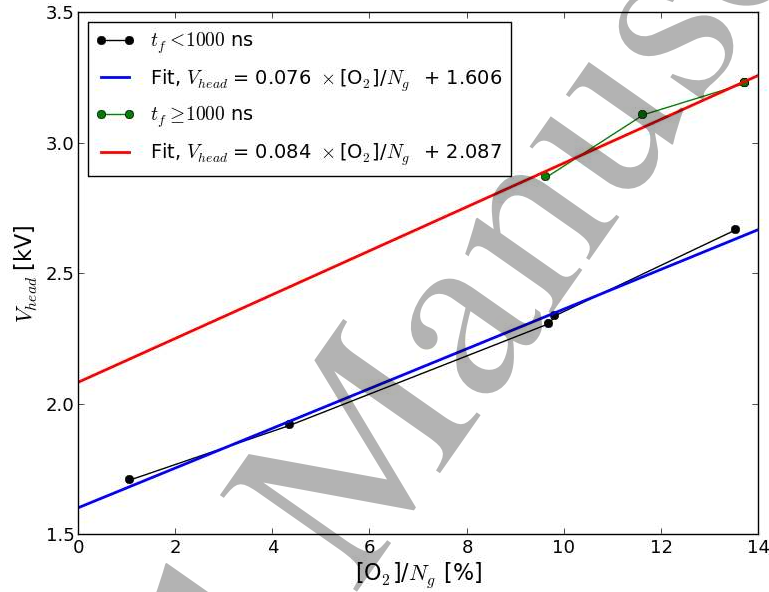where $[O_2]/N_g$ is again in % and V_{head} in kV.

Figure 15. V_{head} at $r = 0$ mm and 0.5 mm behind the position of the maximum of $|E_z|$ when the discharge stops, as function of the relative O_2 density at that position, from simulation results. Linear fits of data with $t_f < 1000$ ns and data with $t_f \geq 1000$ ns are also shown, where V_{head} is in kV and $[O_2]/N_g$ in %.

4. Conclusions

This paper quantitatively characterizes a kHz atmospheric pressure He plasma jet without target powered by a pulse of positive applied voltage. It focuses on a quantitative comparison between experimental measurements and numerical results of a two-dimensional fluid model.

Characterization of a kHz atmospheric pressure plasma jet: ...   30

Experiments have assessed the distribution of number density of N_2 and O_2 in the plasma plume through rotational Raman scattering and have followed the position and velocity of discharge propagation through ICCD imaging. Moreover, the peak electric field in the discharge front has been measured through Stark polarization spectroscopy and the electron density and temperature behind the front have been measured through Thomson scattering. These results have been compared with those of the two-dimensional model using the same configuration. It has been shown that the gas mixture distribution obtained through flow simulations and used in the plasma model agrees with the one measured. Moreover, an agreement of about 80 % has been obtained on discharge velocity and within 5 mm for the length of propagation for different values of magnitude of applied voltage (4 kV and 6 kV) and pulse width (between 300 and 1000 ns). An agreement with a maximum discrepancy of 11 % has been achieved between simulations and experiments on the axial component of electric field in the discharge front propagating inside the tube, of around 10 kV·cm^{-1}, and in the plasma plume up to 2 cm out of the tube, where it rises up to 20 kV·cm^{-1}. The comparison with the simulations suggests that the measured electric field does not correspond to the absolute peak of electric field in the front, but to an average of the axial component of electric field within a distance of 0.1 mm around the axial position of the peak. Moreover, it is the first time that the rise of the electric field in the plume as measured by experiments has been compared quantitatively and agree with results from simulations in the same jet. The comparison of electron density around the discharge front in the plasma plume has provided the same trends in experiments and simulations, with an increase in the plume, but no quantitative agreement. The measurements show an increase of electron density from 0.4×10^{13} cm^{-3} near the tube nozzle up to 2×10^{13} cm^{-3} at a 1 cm distance, while in the simulations the electron density remains between 0.2 and 0.5×10^{13} cm^{-3} in that region. The electron temperature agrees also qualitatively, with a decrease in the plume. Values of electron temperature of up to around 3 eV near the nozzle down to around 0.5 eV at a distance of around 2 cm have been obtained from the experiments, while the simulations provide values of around 4 eV near the nozzle down to around 0.5 eV at around 3.5 cm from the nozzle. The divergence is attributed to the uncertainty in memory effects between pulses and in plasma chemistry coefficients.

We have shown that the values of electron density and temperature depend highly on the position in the jet where they are measured, since both show large

Characterization of a kHz atmospheric pressure plasma jet: ...   31

gradients in radial and axial direction. The simulations results suggest that the location where Thomson scattering measures the electron density and temperature is in the quasi-neutral channel behind the front and not inside the high field front. Therefore, the electron density is higher than in the front and increases along the plume, while the electron temperature is lower and decreases along the plume.

Both experiments and simulations have shown that discharge propagation stops during the pulse in the case of long pulses ($\geq$ 1000 ns width) and by the action of the fall of the pulse in the case of shorter pulses ($<$ 1000 ns width). In fact, the length of discharge propagation has been shortened by decreasing the magnitude of applied voltage and by decreasing pulse width. Measurements and simulations have shown that the electric field in the discharge front is invariable with these parameters. Then, the numerical simulations have assessed the temporal evolution of the electric potential in the discharge head for the different cases. This potential slowly decreases during discharge propagation and is forced to decrease faster at the end of the pulse. Propagation stops when the potential in the discharge head is lower than a certain threshold.

The results suggest that this threshold is defined by the gas mixture at the position of the front. In fact, the peak electric field required to produce free electrons ahead of the discharge front high enough to sustain discharge propagation increases with the air admixture along the plume. On the one hand, that electric field is dependent on the electric potential in the plasma. On the other hand, it is generated by charge separation, which is directly affected by the chemistry in the local gas-mixture. Hence, the combination of the two factors determines if a high enough electric field can take place to sustain discharge propagation. The relationship between threshold potential in the discharge head required to sustain propagation and local relative oxygen density has been derived for the cases of short and long pulses.

Acknowledgments

Characterization of a kHz atmospheric pressure plasma jet: ...   32

References

[1] D. Graves, "Low temperature plasma biomedicine: A tutorial review," *Physics of Plasmas (1994-present)*, vol. 21, no. 8, p. 080901, 2014.

[2] M. Ito, J.-S. Oh, T. Ohta, M. Shiratani, and M. Hori, "Current status and future prospects of agricultural applications using atmospheric-pressure plasma technologies," *Plasma Processes and Polymers*, vol. 15, p. 1700073, feb 2018.

[3] C. Cheng, Z. Liye, and R.-J. Zhan, "Surface modification of polymer fibre by the new atmospheric pressure cold plasma jet," *Surface and Coatings Technology*, vol. 200, pp. 6659–6665, aug 2006.

[4] G. B. Sretenović, I. B. Krstić, V. V. Kovačević, B. M. Obradović, and M. M. Kuraica, "Spectroscopic measurement of electric field in atmospheric-pressure plasma jet operating in bullet mode," *Applied Physics Letters*, vol. 99, p. 161502, oct 2011.

[5] S. Hübner, J. S. Sousa, V. Puech, G. M. W. Kroesen, and N. Sadeghi, "Electron properties in an atmospheric helium plasma jet determined by Thomson scattering," *Journal of Physics D: Applied Physics*, vol. 47, p. 432001, oct 2014.

[6] C. Jiang, J. Miles, J. Hornef, C. Carter, and S. Adams, "Electron densities and temperatures of an atmospheric-pressure nanosecond pulsed helium plasma jet in air," *Plasma Sources Science and Technology*, vol. 28, p. 085009, aug 2019.

[7] S. Hübner, J. S. Sousa, J. van der Mullen, and W. G. Graham, "Thomson scattering on non-thermal atmospheric pressure plasma jets," *Plasma Sources Science and Technology*, vol. 24, p. 054005, jan 2017.

[8] Y. Sakiyama, D. B. Graves, and E. Stoffels, "Influence of electrical properties of treated surface on RF-excited plasma needle at atmospheric pressure," *Journal of Physics D: Applied Physics*, vol. 41, p. 095204, may 2008.

[9] Z. Xiong, E. Robert, V. Sarron, J.-M. Pouvesle, and M. J. Kushner, "Dynamics of ionization wave splitting and merging of atmospheric-pressure plasmas in branched dielectric tubes and channels," *Journal of Physics D: Applied Physics*, vol. 45, p. 275201, jul 2012.

[10] R. Wang, C. Zhang, Y. Shen, W. Zhu, P. Yan, T. Shao, N. Y. Babaeva, and G. V. Naidis, "Temporal and spatial profiles of emission intensities in atmospheric pressure helium plasma jet driven by microsecond pulse: Experiment and simulation," *Journal of Applied Physics*, vol. 118, p. 123303, sep 2015.

Characterization of a kHz atmospheric pressure plasma jet: ...   33

[11] A. M. Lietz, E. Johnsen, and M. J. Kushner, "Plasma-induced flow instabilities in atmospheric pressure plasma jets," *Applied Physics Letters*, vol. 111, p. 114101, sep 2017.

[12] W. Ning, D. Dai, Y. Zhang, Y. Han, and L. Li, "Effects of trace of nitrogen on the helium atmospheric pressure plasma jet interacting with a dielectric substrate," *Journal of Physics D: Applied Physics*, vol. 51, p. 125204, mar 2018.

[13] C. Lazarou, C. Anastassiou, I. Topala, A. S. Chiper, I. Mihaila, V. Pohoata, and G. E. Georghiou, "Numerical simulation of capillary helium and helium–oxygen atmospheric pressure plasma jets: propagation dynamics and interaction with dielectric," *Plasma Sources Science and Technology*, vol. 27, p. 105007, oct 2018.

[14] A. Bourdon, T. Darny, F. Pechereau, J.-M. Pouvesle, P. Viegas, S. Iséni, and E. Robert, "Numerical and experimental study of the dynamics of a μ s helium plasma gun discharge with various amounts of N 2 admixture," *Plasma Sources Science and Technology*, vol. 25, p. 035002, jun 2016.

[15] L. Ji, W. Yan, Y. Xia, and D. Liu, "The effect of target materials on the propagation of atmospheric-pressure plasma jets," *Journal of Applied Physics*, vol. 123, p. 183302, may 2018.

[16] P. Zhu, B. Li, Z. Duan, and J. Ouyang, "Development from dielectric barrier discharge to atmospheric pressure plasma jet in helium: experiment and fluid modeling," *Journal of Physics D: Applied Physics*, vol. 51, p. 405202, oct 2018.

[17] P. Viegas, F. Péchereau, and A. Bourdon, "Numerical study on the time evolutions of the electric field in helium plasma jets with positive and negative polarities," *Plasma Sources Science and Technology*, vol. 27, p. 025007, feb 2018.

[18] E. Slikboer, P. Viegas, Z. Bonaventura, E. Garcia-Caurel, A. Sobota, A. Bourdon, and O. Guaitella, "Experimental and numerical investigation of the transient charging of a dielectric surface exposed to a plasma jet," *Plasma Sources Science and Technology*, vol. 28, p. 095016, sep 2019.

[19] B. L. Sands, B. N. Ganguly, and K. Tachibana, "A streamer-like atmospheric pressure plasma jet," *Applied Physics Letters*, vol. 92, p. 151503, apr 2008.

[20] G. V. Naidis, "Modelling of streamer propagation in atmospheric-pressure helium plasma jets," *Journal of Physics D: Applied Physics*, vol. 43, p. 402001, oct 2010.

[21] G. V. Naidis, "Modelling of plasma bullet propagation along a helium jet in ambient air," *Journal of Physics D: Applied Physics*, vol. 44, p. 215203, jun 2011.

[22] D. Breden, K. Miki, and L. L. Raja, "Computational study of cold atmospheric nanosecond pulsed helium plasma jet in air," *Applied Physics Letters*, vol. 99, p. 111501, sep 2011.

[23] D. Breden, K. Miki, and L. L. Raja, "Self-consistent two-dimensional modeling of cold atmospheric-pressure plasma jets/bullets," *Plasma Sources Science and Technology*, vol. 21, p. 034011, jun 2012.

[24] J.-P. Boeuf, L. L. Yang, and L. C. Pitchford, "Dynamics of a guided streamer ('plasma bullet') in a helium jet in air at atmospheric pressure," *Journal of Physics D: Applied Physics*, vol. 46, p. 015201, jan 2013.

[25] N. Y. Babaeva and G. V. Naidis, "Two-dimensional modelling of positive streamer dynamics in non-uniform electric fields in air," *Journal of Physics D: Applied Physics*, vol. 29, pp. 2423–

Characterization of a kHz atmospheric pressure plasma jet: ...   34

2431, sep 1996.

[26] A. A. Kulikovsky, "Positive streamer between parallel plate electrodes in atmospheric pressure air," *Journal of Physics D: Applied Physics*, vol. 30, pp. 441–450, feb 1997.

[27] N. Mericam-Bourdet, M. Laroussi, A. Begum, and E. Karakas, "Experimental investigations of plasma bullets," *Journal of Physics D: Applied Physics*, vol. 42, p. 055207, mar 2009.

[28] G. V. Naidis, "Modeling of helium plasma jets emerged into ambient air: Influence of applied voltage, jet radius, and helium flow velocity on plasma jet characteristics," *Journal of Applied Physics*, vol. 112, p. 103304, nov 2012.

[29] A. Shashurin, M. N. Shneider, and M. Keidar, "Measurements of streamer head potential and conductivity of streamer column in cold nonequilibrium atmospheric plasmas," *Plasma Sources Science and Technology*, vol. 21, p. 034006, jun 2012.

[30] A. Sobota, O. Guaitella, G. B. Sretenović, I. B. Krstić, V. V. Kovačević, A. Obrusník, Y. N. Nguyen, L. Zajíčková, B. M. Obradović, and M. M. Kuraica, "Electric field measurements in a kHz-driven He jet—the influence of the gas flow speed," *Plasma Sources Science and Technology*, vol. 25, p. 065026, nov 2016.

[31] E. Slikboer, O. Guaitella, and A. Sobota, "Time-resolved electric field measurements during and after the initialization of a kHz plasma jet—from streamers to guided streamers," *Plasma Sources Science and Technology*, vol. 25, p. 03LT04, jun 2016.

[32] M. Hofmans and A. Sobota, "Influence of a target on the electric field profile in a kHz atmospheric pressure plasma jet with the full calculation of the Stark shifts," *Journal of Applied Physics*, vol. 125, p. 043303, jan 2019.

[33] B. L. M. Klarenaar, O. Guaitella, R. Engeln, and A. Sobota, "How dielectric, metallic and liquid targets influence the evolution of electron properties in a pulsed He jet measured by Thomson and Raman scattering," *Plasma Sources Science and Technology*, vol. 27, p. 085004, aug 2018.

[34] B. L. M. Klarenaar, F. Brehmer, S. Welzel, H. J. van der Meiden, M. C. M. van de Sanden, and R. Engeln, "Note: Rotational Raman scattering on CO 2 plasma using a volume Bragg grating as a notch filter," *Review of Scientific Instruments*, vol. 86, p. 046106, apr 2015.

[35] B. L. M. Klarenaar, M. Grofulović, A. S. Morillo-Candas, D. C. M. van den Bekerom, M. A. Damen, M. C. M. van de Sanden, O. Guaitella, and R. Engeln, "A rotational Raman study under non-thermal conditions in a pulsed CO 2 glow discharge," *Plasma Sources Science and Technology*, vol. 27, p. 045009, apr 2018.

[36] A. F. H. van Gessel, E. A. D. Carbone, P. J. Bruggeman, and J. J. A. M. van der Mullen, "Laser scattering on an atmospheric pressure plasma jet: disentangling Rayleigh, Raman and Thomson scattering," *Plasma Sources Science and Technology*, vol. 21, p. 015003, feb 2012.

[37] P. Viegas and A. Bourdon, "Numerical study of jet-target interaction: influence of dielectric permittivity on the electric field experienced by the target," *accepted on Plasma Chemistry and Plasma Processing*, 2019. https://doi.org/10.1007/s11090-019-10033-6.

[38] COMSOL, "CFD module user's guide, version 5.3," 2016. www.comsol.com/cfd-module.

[39] P. Viegas, *Electric field characterization of atmospheric pressure helium plasma jets through numerical simulations and comparisons with experiments.* Ph. D. thesis, École

Characterization of a kHz atmospheric pressure plasma jet: ...   35

Polytechnique, France, 2018. http://www.theses.fr/2018SACLX061.

[40] J. Winter, J. S. Sousa, N. Sadeghi, A. Schmidt-Bleker, S. Reuter, and V. Puech, "The spatio-temporal distribution of He (2 3 S 1) metastable atoms in a MHz-driven helium plasma jet is influenced by the oxygen/nitrogen ratio of the surrounding atmosphere," *Plasma Sources Science and Technology*, vol. 24, p. 025015, mar 2015.

[41] A. Schmidt-Bleker, S. Reuter, and K.-D. Weltmann, "Quantitative schlieren diagnostics for the determination of ambient species density, gas temperature and calorimetric power of cold atmospheric plasma jets," *Journal of Physics D: Applied Physics*, vol. 48, p. 175202, may 2015.

[42] G. Hagelaar and L. Pitchford, "Solving the Boltzmann equation to obtain electron transport coefficients and rate coefficients for fluid models," *Plasma Sources Science and Technology*, vol. 14, no. 722, 2005.

[43] S. Pancheshnyi, S. Biagi, M. Bordage, G. Hagelaar, W. Morgan, A. Phelps, and L. Pitchford, "The LXCat project: Electron scattering cross sections and swarm parameters for low temperature plasma modeling," *Chemical Physics*, vol. 398, p. 148, 2012.

[44] IST, "IST-Lisbon database," 2018. www.lxcat.net, retrieved on January 2018.

[45] E. Slikboer, E. Garcia-Caurel, O. Guaitella, and A. Sobota, "Charge transfer to a dielectric target by guided ionization waves using electric field measurements," *Plasma Sources Science and Technology*, vol. 26, p. 035002, feb 2017.

[46] A. Begum, M. Laroussi, and M. R. Pervez, "Atmospheric pressure He-air plasma jet: Breakdown process and propagation phenomenon," *AIP Advances*, vol. 3, p. 062117, jun 2013.

[47] D. Maletić, N. Puač, N. Selaković, S. Lazović, G. Malović, A. Dordević, and Z. L. Petrović, "Time-resolved optical emission imaging of an atmospheric plasma jet for different electrode positions with a constant electrode gap," *Plasma Sources Science and Technology*, vol. 24, p. 025006, feb 2015.

[48] J. Jarrige, M. Laroussi, and E. Karakas, "Formation and dynamics of plasma bullets in a non-thermal plasma jet: influence of the high-voltage parameters on the plume characteristics," *Plasma Sources Science and Technology*, vol. 19, p. 065005, dec 2010.

[49] G. V. Naidis and J. L. Walsh, "The effects of an external electric field on the dynamics of cold plasma jets—experimental and computational studies," *Journal of Physics D: Applied Physics*, vol. 46, p. 095203, mar 2013.

[50] J. Jánský and A. Bourdon, "Simulation of helium discharge ignition and dynamics in thin tubes at atmospheric pressure," *Applied Physics Letters*, vol. 99, p. 161504, oct 2011.

[51] P. Olszewski, E. Wagenaars, K. McKay, J. W. Bradley, and J. L. Walsh, "Measurement and control of the streamer head electric field in an atmospheric-pressure dielectric barrier plasma jet," *Plasma Sources Science and Technology*, vol. 23, p. 015010, feb 2014.

[52] G. B. Sretenović, I. B. Krstić, V. V. Kovačević, B. M. Obradović, and M. M. Kuraica, "Spatio-temporally resolved electric field measurements in helium plasma jet," *Journal of Physics D: Applied Physics*, vol. 47, p. 102001, mar 2014.

[53] G. B. Sretenović, O. Guaitella, A. Sobota, I. B. Krstić, V. V. Kovačević, B. M. Obradović, and M. M. Kuraica, "Electric field measurement in the dielectric tube of helium atmospheric

Characterization of a kHz atmospheric pressure plasma jet: ... 36

pressure plasma jet," *Journal of Applied Physics*, vol. 121, p. 123304, mar 2017.

[54] N. Y. Babaeva, G. V. Naidis, V. A. Panov, R. Wang, S. Zhang, C. Zhang, and T. Shao, "Plasma bullet propagation and reflection from metallic and dielectric targets," *Plasma Sources Science and Technology*, vol. 28, p. 095006, sep 2019.

[55] A. M. Lietz and M. J. Kushner, "Molecular admixtures and impurities in atmospheric pressure plasma jets," *Journal of Applied Physics*, vol. 124, p. 153303, oct 2018.

[56] S. A. Norberg, E. Johnsen, and M. J. Kushner, "Helium atmospheric pressure plasma jets interacting with wet cells: delivery of electric fields," *Journal of Physics D: Applied Physics*, vol. 49, p. 185201, may 2016.

[57] C.-G. Schregel, E. A. D. Carbone, D. Luggenhölscher, and U. Czarnetzki, "Ignition and afterglow dynamics of a high pressure nanosecond pulsed helium micro-discharge: I. Electron, Rydberg molecules and He (2 3 S) densities," *Plasma Sources Science and Technology*, vol. 25, p. 054003, sep 2016.